Neutron radiography of a static density gradient of 3He gas at cryogenic temperatures

Journal Article

Author(s):
Wichmann, Gunther; Antognini, Aldo; Eggenberger, Andreas; Kirch, Klaus Stefan (iD); Piegsa, Florian M.; Solèr, Ursin (iD); Stahn, J.; Taqqu, David

Neutron radiography of a static density gradient of ^{3}He gas at cryogenic temperatures

G. Wichmann [a], A. Antognini [a,b], A. Eggenberger [a], K. Kirch [a,b], F.M. Piegsa [a], U. Soler [a], J. Stahn [b], D. Taqqu [a]

[a] Institute for Particle Physics, ETH Zurich, Switzerland
[b] Paul Scherrer Institute, Villigen, Switzerland

ARTICLE INFO

ABSTRACT

We demonstrate a stationary helium gas density gradient which is needed for a proposed novel low-energy μ^+ beam line. In a closed system with constant pressure the corresponding density gradient is only a function of the temperature. In a neutron radiography experiment two gas cells with different geometries were filled with ^{3}He gas at constant pressures of about 10 mbar. Temperatures in the range from 6 K to 40 K were applied and density distributions with a maximum to minimum density ratio of larger than 3 were realized. The distribution was investigated employing the strongly neutron absorbing isotope ^{3}He. A simple one-dimensional approach derived from Fourier's law describes the obtained gas density with a deviation $< 2\%$.

1. Introduction

Many experiments and applications would greatly benefit from improved muon beams with small phase space volume or will become possible once efficient muon cooling procedures have been established. Cooling muons is especially challenging due to their short lifetime of 2.2 μs. Depending on the aimed application (e.g. a muon storage ring, muon spin rotation, muonium spectroscopy) different approaches are being studied, e.g. ionization cooling of the muon beam (MICE) [1], particle detection and steering [2], or frictional cooling [3]. A recently proposed concept [4] of a novel low-energy muon beam line aims at converting MeV muons into eV or sub-eV muons and compressing the spatial distribution yielding an overall phase space compression of 10 orders of magnitude with a yield of about 10^{-3} mainly limited by the muon decay. The concept can be divided into three separate sections: transverse compression, longitudinal compression, and extraction into vacuum. Longitudinal beam compression has recently been demonstrated by our group [5]. Here only the transverse compression is considered and in particular, the requirement to establish a gas target with a large stationary, vertical density gradient.

The starting point is an existing muon beam with muon momenta < 10 MeV/c, e.g. πE1 beam line at the Paul Scherrer Institute, Villigen, Switzerland. A fraction of the incident muon beam is stopped in helium gas with a stationary density gradient in vertical direction. Helium is chosen because it is inert to μ^+ (small fraction of muonium production). The required density ratio at the bottom of the target to the one at the top is about 3. The stopped muons are distributed in the gas over regions of different density. The drift vectors of the initially stopped muons strongly depend on the applied electric field (about 2 kV/cm), the magnetic field (5 T) and the mean time between collisions with the gas. For suitable field directions and parameters the stopped muons in the upper part of the cell with lower gas density drift downwards and muons stopped in the bottom part with higher gas density drift upwards. This causes a compression of the stopped muon cloud into a smaller volume. A detailed description of the physical process can be found in [4,5]. The similarity of ^{3}He and ^{4}He gas enables the investigation of the density by neutron radiography of ^{3}He and the use of the conclusions to ^{4}He. This paper describes the realization of the required density gradient in a cryogenic ^{3}He gas target and its visualization using neutron radiography.

2. Temperature function $T(y)$

A stationary density gradient of ^{3}He gas (purity $\geq 99.7\%$) is realized by a temperature $T(y)$ with a gradient in vertical direction y (along gravity) and a constant pressure p. This results in a

spatially dependent density. The ideal gas equation can be used for cryogenic temperatures down to 6 K because low pressures of about 10 mbar result in a sufficiently small contribution from the second virial coefficient $< 0.2\%$ for $< 100\ cm^3/mol$ [6]. This connects the temperature $T(y)$ to the number density $n(y)$:

$$n(y) = \frac{N}{V} = \frac{p}{k_B \cdot T(y)} \qquad (1)$$

with k_B being the Boltzmann constant, N the number of particles, V the volume and p the pressure. From Eq. (1) it follows that the maximum to minimum number density ratio is proportional to the temperature ratio:

$$\frac{n_{max}}{n_{min}} = \frac{n(y=min)}{n(y=max)} = \frac{T(y=max)}{T(y=min)} = \frac{T_{high}}{T_{low}} \qquad (2)$$

This indicates the advantage of using cryogenic temperatures to obtain large density ratios.

$T(y)$ is realized by a constant heat flux $\dot{q}$ through the ^{3}He gas. Fourier's law for the temperature gradient ∇T and the heat flux $\dot{q}$ holds:

$$\dot{q} = k(T) \cdot \nabla T = k(T(y)) \cdot \frac{dT(y)}{dy} \qquad (3)$$

with $k = k(T)$ the temperature-dependent thermal conductivity of the gas. The temperature $T(y)$ for $y \in [0, h]$ within a gas cell of height h is defined by the two temperatures $T(y=0) = T_{low}$ and $T(y=h) = T_{high}$ of the gas cell. For a wide range of pressures, valid here, the thermal conductivity $k(T)$ of ^{4}He gas in the range from 4 K to 40 K and of ^{3}He gas from 6 K to 40 K can be parametrized with:

$$k(T) = a \cdot T^b \quad \left[\frac{W}{m \cdot K}\right] \qquad (4)$$

For colder temperatures the conductivity differs significantly from Eq. (4), but is in good agreement for ^{4}He above 4 K and for ^{3}He above 6 K. For ^{4}He gas the parameters are fitted to ab-initio calculations from [7] and in agreement with measured values [8]:

$$a = 0.00336(7) \quad \left[\frac{W}{m \cdot K^{b+1}}\right], \quad b = 0.683(7)$$

For ^{3}He gas the parameters are fitted to ab-initio calculations from [9]:

$$a = 0.00483(5) \quad \left[\frac{W}{m \cdot K^{b+1}}\right], \quad b = 0.620(3)$$

The stationary heat equation restricted to one dimension and with the given parameterized thermal conductivity $k(T)$ holds:

$$0 = \nabla \cdot (k(T)\nabla T) = \nabla k(T) \cdot \nabla T + k(T)\Delta T = \frac{dk(T)}{dT}\nabla T \cdot \nabla T$$

$$+ k(T)\Delta T = b \cdot \frac{k(T)}{T}\left(\frac{dT}{dy}\right)^2 + k(T)\frac{d^2T}{dy^2} \qquad (5)$$

This results in an analytic function for the temperature:

$$T(y, h) = \Delta T \cdot (y/h)^{1/(1+b)} + T_{low} \qquad (6)$$

with $\Delta T = T_{high} - T_{low} > 0$ and y the vertical position in the gas $(0 \le y \le h)$. Combining Eqs. (6) and (1) the number density of the gas for a constant vertical heat flux through a gas cell with height h neglecting wall effects is obtained

$$n(y; h) = \frac{p}{k_B \cdot T(y, h)}. \qquad (7)$$

3. Experiment

3.1. Cryogenic setup and gas cells

For cooling to cryogenic temperatures a pulse tube refrigerator[1] was used with nominal cooling powers for the 1st stage of 40 W at 45 K and for the 2nd stage of 1.5 W at 4.2 K. Two gas cells were thermally coupled to the 2nd stage and placed in a vacuum chamber with pressure $\le 10^{-6}$ mbar and inside a thermal radiation shield kept at a temperature below 60 K by the 1st stage of the cryocooler.

Two gas cells were built (see Fig. 1): One with a rectangular cross-section (A) and one with a wedge-shaped cross-section (B). Cell A has horizontal bottom and top plates resulting in a cuboid gas region with a width and height of 40 mm. Cell B has inclined bottom and top plates. Hence the height h in cell B depends on the lateral x position: $h = h(x)$. Both cells have a length of $L = 200$ mm. The shape of Cell B is similar to the envisaged design for the target cell for transverse muon compression (cf. Fig. 1 of [4]). The cells have side walls of stainless steel with a thickness of only about 0.8 mm in order to reduce heat flow through the walls. The bottom and top plates made of copper create uniform temperature boundaries T_{low} at the bottom and T_{high} at the top. The bottom plate is thermally anchored to the cryocooler. When no heating is applied it reaches approximately 4 K. The entire setup is cooled down from room to base temperature within 8 h. To achieve various temperature functions electrical resistors for heating are mounted on the top plate. After switching on the heating a stationary state is reached within 2–3 h. A photo of the cells is presented in Fig. 2.

3.2. Neutron radiography

The neutron radiography measurements were performed at the cold neutron beam line 'Morpheus' at the Swiss Spallation Neutron Source (SINQ). The Morpheus beam line provides monochromatic neutrons with a de Broglie wavelength of $\lambda = 5$ Å, i.e. a velocity of 790 m/s. The absorption cross-section for ^{3}He is then $\sigma_{abs} \approx 14,800$ b ($\sigma_{abs} = 5333(7)$b for thermal neutrons with $\lambda = 1.81$ Å [10]). ^{3}He gas was used because of its strong neutron absorption and the thermodynamic similarity to ^{4}He gas.[2] For measurements a basic pinhole imaging setup was used (see Fig. 3). The neutrons travel from the beam aperture (opening 3 mm $\times$ 3 mm) to the image plate (distance $z_{ip} = 2.2$ m). The monitor[3] behind the aperture is used for beam normalization in order to potentially suppress beam intensity fluctuations. The vacuum chamber containing the gas cells is positioned between the aperture and the image plate. The maximal distance of the cells to the image plate is 0.4 m (entrance window of the cells), the minimal distance is 0.2 m (exit window of the cells). This results in a geometric resolution of about 0.7 mm and a magnification on the image plate of the projected entrance window of $+20\%$ and for the exit window of $+10\%$.

The image plate is sensitive to neutrons due to Gadolinium serving as a converter [11,12]. The photostimulated luminescence (PSL) is linearly dependent on the amount of incident neutrons. This was confirmed by taking open beam images, i.e. without vacuum chamber and gas cells between aperture and image plate. The image plate was then exposed for different durations from 3 min to 20 min. For the open beam setup, the image plate is exposed to an approximately uniform distributed number of

---

[1] PT415 from Cryomech, Inc.
[2] cf. Eq. (4)
[3] Fission chamber from LND, Inc. with an efficiency of approximately 10^{-4}.

neutrons per area for the central area of the beam spot up to a size of 8 mm × 8 mm. The exposed image plates were read out with a dedicated scanner. The scanned images have a pixel size of 0.1 mm × 0.1 mm. The read out value of a single pixel is the intensity I. The intensity measured in the various pixels in the central region of the image plate shows a Gaussian distribution
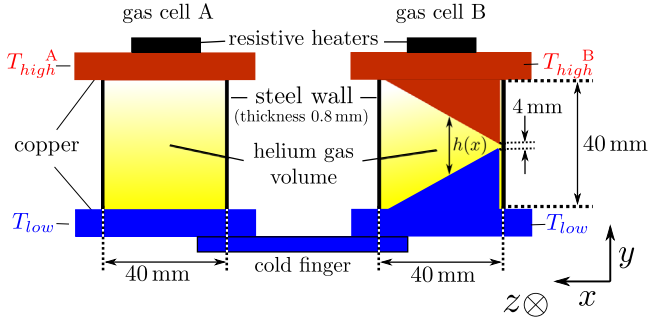

Fig. 1. Scheme of gas cells A and B. The helium gas volume of each cell is limited by a copper plate on top and bottom, and thin side walls of stainless steel with a thickness of 0.8 mm. The bottom plates are mounted on the cold finger of the cryocooler. Resistive heaters are mounted on the top plates. Gas cell B has an inclined top and bottom resulting in a height $h(x)$ dependent on the lateral position x. Both cells have a length $L = 200$ mm in neutron beam direction (z-direction).
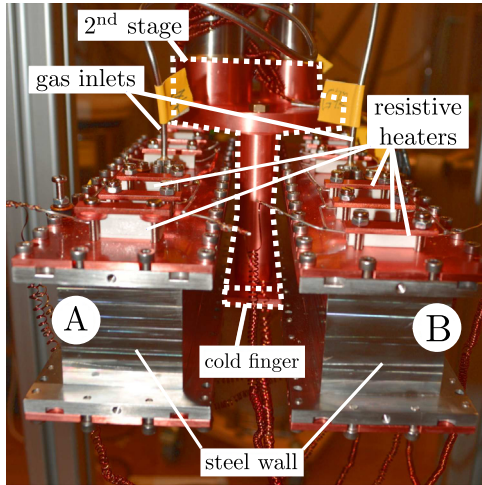

Fig. 2. Photo of gas cell A and B. The cold finger is mounted onto the 2nd stage of the cryocooler. The middle part of the cells is a frame of stainless steel sealed with the bottom and top copper plates containing the gas volume. The gas inlets and resistive heaters are attached to the top plates.

with mean intensity $\bar{I}$ and standard deviation $\sigma(\bar{I})$. For $\bar{I}$ as a function of the amount of exposed neutrons a calibration factor was measured:

$$\bar{I} = 1.67(1) \cdot (\text{neutron monitor count}/10^6) \tag{8}$$

where 10^6 monitor counts correspond to an exposure of 5 min for a constant proton beam current of about 1.5 mA on the SINQ target. A fit of $\sigma(\bar{I})$ for different exposure times results in an estimated statistical error for the intensity:

$$\sigma(\bar{I}) = 0.206(1) \cdot \sqrt{\bar{I}} \tag{9}$$

4. Data processing

In the data processing two different Cartesian coordinates are distinguished. One is aligned with the gas cell (cf. Fig. 1) and labeled with 'cell' ($\vec{x}_{cell}$, $\vec{y}_{cell}$ and $\vec{z}_{cell}$). The other ($\vec{x}$, $\vec{y}$ and $\vec{z}$) is oriented along the central axis of the neutron beam and the perpendicular image plate (cf. Fig. 3). For a perfectly aligned gas cell, the corresponding basis vectors would point in the same directions.

To measure the density gradient an image, $I(x_i, y_i)$, of a cell filled with ^{3}He gas is used together with an image, $I_0(x_i, y_i)$, of the empty cell (cf. Figs. 4 and 5). To each image $I(x_i, y_i)$ corresponds a measurement of the temperature T_{low}, T_{high} and the pressure p in the filled cell. Due to positioning uncertainty of the image plates, each image has an independent misalignment in x and y and a rotation around the z-axis. Alignment of the various images has been performed offline by identifying and adjusting the position of well-defined edges of the taken images (see Fig. 6).

The neutron radiography measures the transmission of the neutrons through the ^{3}He gas, described by Beer–Lambert's law:

$$I(x,y) = I_0(x,y) \cdot \exp\left[-\sigma_{abs} \cdot \int_\gamma n(x_{cell}, y_{cell}, z_{cell})\, ds \right] \tag{10}$$

with $n(x_{cell}, y_{cell}, z_{cell})$ the number density of the ^{3}He gas, σ_{abs} the absorption cross-section, γ the neutron path, $I(x, y)$ the transmission of the neutrons through the gas cell filled with ^{3}He gas and $I_0(x, y)$ the transmission through the empty gas cell. The averaged number density of the ^{3}He gas can be obtained with

$$\bar{n}(x_i, y_i) := 1/L \cdot \int_\gamma n(x_{cell}, y_{cell}, z_{cell})\, ds = -1/(\sigma_{abs} \cdot L)$$
$$\cdot \ln\left[I(x_i, y_i)/I_0(x_i, y_i) \right] \tag{11}$$
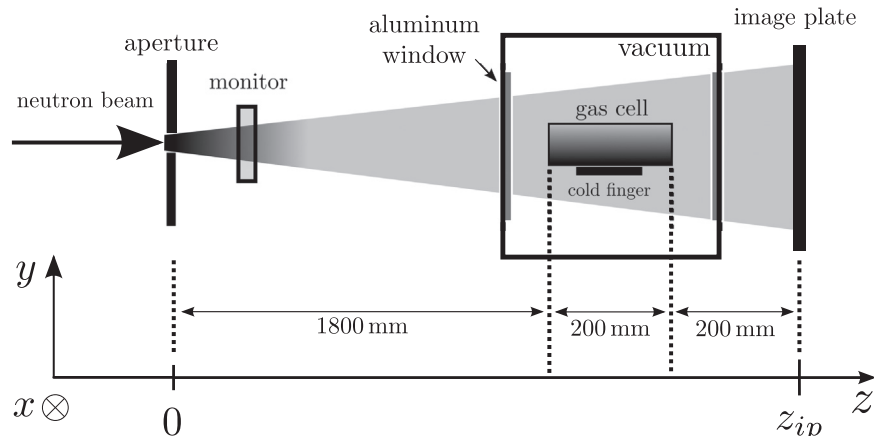
with L the length of the gas cell.

Fig. 3. Neutron radiography setup at Morpheus beam line (SINQ, Paul Scherrer Institute). From left: Monochromatic neutron beam ($\lambda = 5$ Å), beam aperture (square of 3 mm × 3 mm), monitor (detector), entrance window to the vacuum chamber (aluminum window), gas cell, exit window of the vacuum chamber, and the image plate.
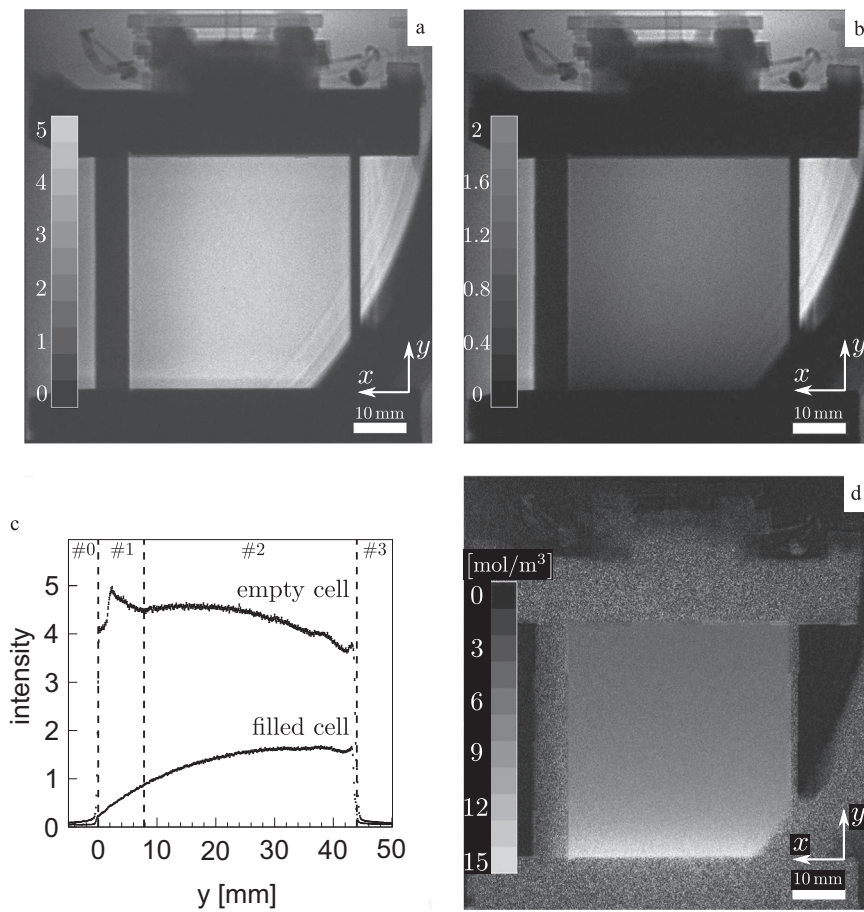
Fig. 4. Neutron radiographies of cell A: (a) empty cell, (b) filled with ^{3}He, (c) average intensity of (a) and (b) in vertical direction, and (d) obtained number density. The lower right corner of the images is shadowed by the edges of the aluminum windows of the vacuum chamber. In (a) and (b) a bar with intensities I proportional to the transmission in arbitrary but identical units is shown. In (c) four ranges are indicated: #0: shadowed by the bottom plate, #1: affected by neutron reflection, #2: transmission with only minor neutron reflections, #3: shadowed by the top plate. In (d) the number density for gradient III from Table 1 is shown.
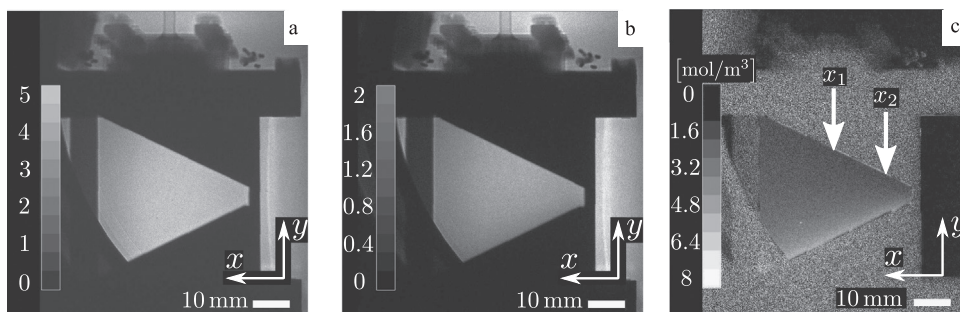

Fig. 5. Neutron radiographies of cell B: (a) empty cell, (b) filled with ^{3}He and (c) obtained number density. The lower left corner of the images is shadowed by the edges of the aluminum windows of the vacuum chamber. On (a) and (b) a bar with intensities I proportional to the transmission in arbitrary but identical units is shown. On (c) the number density with setting from Table 1 is shown. The lateral position corresponding to a height of about 20 mm (middle of the cell) and to a height of about 10 mm is indicated with 'x_1' and 'x_2', respectively.

In general the neutron path is passing differently dense regions of the gas cell even for a number density constant in z_{cell}-direction due to beam divergence. Therefore forward calculations were done to connect the experimentally observed $\overline{n}(x_i, y_i)$ from Eq. (11) to the number density in the gas cell $n(x_{cell}, y_{cell}, z_{cell})$ by using the expected number density $n(y_{cell}; h)$ from Eq. (7):

$$\overline{n}^{sim}(x_i, y_i) := 1/L \cdot \int_{\gamma(x_i, y_i)} n(y_{cell} - y_0; h)\, ds \qquad (12)$$

with $\gamma(x_i, y_i)$ the neutron path between the aperture and the point (x_i, y_i) on the image plate, $y_0 = y_0(x_{cell})$ the bottom of the gas volume and $h = h(x_{cell})$ the height at the lateral position x_{cell}.

4.1. Systematic effects

The contribution to the intensity I_{BKG} of a pixel on the image plate from different origin than the monochromatic neutrons (e.g. gamma radiation) causes background ($I = I_{neutron} + I_{BKG}$). An upper limit of $I_{BKG} = 0.005$ is obtained on the image plate by the regions shielded from the neutron beam by the copper plates of the gas cells. Therefore the constant background is neglected compared to used intensities in the range of $I = 0.3$–8.

The opening of the aperture is 3 mm $\times$ 3 mm. The simplified treatment as a point source generates a systematic error for the forward calculations. The caused error in the number density is
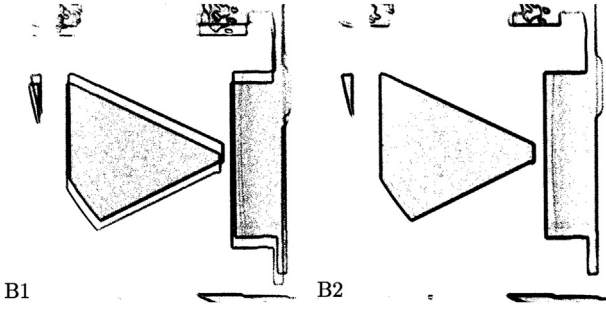
Fig. 6. Superposition of two images filtered with edge-detection. Left image (B1) prior and right image (B2) after alignment procedure.

estimated by calculations with shifted aperture positions. The maximal error deduced from this is below 1.7% and the mean error below 0.5% on the extracted densities.

The nominal neutron wavelength is 5 Å. The averaged number density from Eq. (11) is proportional to $1/\sigma_{abs}$ and therefore proportional to the neutron velocity. The systematic error for the measurement of the density caused by the uncertainty of the absolute neutron wavelength is generously estimated to be $< 2\%$. The relative density for the maximum to minimum ratio stays unaffected from this constant scale factor.

Neutrons can in principle be reflected from the top and bottom plates and the side walls of the cell. Reflected neutrons describe a different path and hence correspond to a different averaged gas density than the non-reflected neutrons. Reflection is not considered by the forward calculation. Therefore the observed number density deviates from the forward calculation where the contribution of reflected neutrons is relevant. Strongly affected areas have been identified in images of the empty cell. To avoid this complication the experimental values $\overline{n}(x_i, y_i)$ are fitted with the simulated values $\overline{n}^{\text{sim}}(x_i, y_i)$ to data for heights > 8 mm above the bottom plate (range #2). The excluded range for heights $y_i - y_0 < 8$ mm is labeled with #1, see Fig. 4(c). In the upper part near the top plate $y_i - y_0 > 35$ mm reflected neutrons are also apparent. However this error is $< 1\%$ due to a smaller amount of reflected neutrons and to a smaller density gradient compared to the bottom plate. The reflected neutrons on the top plate result in a large χ^2 in range #2. Excluding the upper part reduces the sensitivity of the measurement for the parameters T_{low}, T_{high} and b from Eq. (6). Instead the complete range #2 was used with statistical error scaled to achieve $\chi^2 = 1$.

5. Results and discussion

The neutron radiography images yields the density gradients for ^{3}He gas in cell A and B (see Figs. 4 and 5). The number densities in the cells decrease monotonically in vertical direction. With a one dimensional approach of Fourier's law, an equation for the number density is derived (Eq. (7)). The forward calculation of the neutron paths through the setup with this number density fitted to the measurements shows good agreement when areas affected by neutron reflection are excluded. The free fit parameters are the temperatures T_{low} and T_{high}, the pressure p in the cell and the parameter b of the thermal conductivity from Eq. (4) (see rows '2:' in Table 1). The ratio $\overline{n}_{max}/\overline{n}_{min}$ in Table 1 is the maximal observed ratio $\overline{n}(y \approx 0)/\overline{n}(y \approx h)$. The full ratio $T_{\text{high}}/T_{\text{low}}$ is not observable due to the neutron beam divergence. However, because of the good agreement of the measurements and the description derived from the ideal gas equation in range #2 we conclude that the realized density gradient follows Eq. (7) over the whole gas region and that the density ratios equals the temperature ratios.

Table 1

Various settings of T_{low}, T_{high} and p from gas cell A and B. '1:' data from sensor measurement (temperature and pressure) and expected density ratio $n_{max}/n_{min} = T_{\text{high}}/T_{\text{low}}$. '2:' fit values of the forward calculation to the measurement, asymptotic standard error in brackets; T_{low}, T_{high}, and the parameter for the thermal conductivity b from Eq. (4) ($b = 0.620(3)$ from ab-initio data) and the maximal observed ratio $\overline{n}_{max}/\overline{n}_{min} = \overline{n}(y \approx 0)_{\Delta x}/\overline{n}(y \approx h)_{\Delta x}$. The full ratio $T_{\text{high}}/T_{\text{low}}$ is not observable because of the neutron beam divergence.

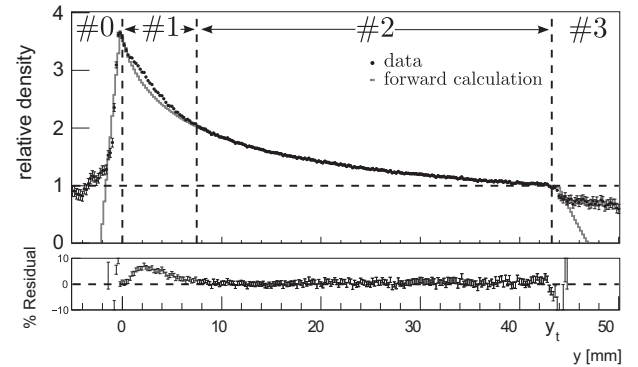| Settings	T_{low}/K	T_{high}/K	p/mbar	b	$\dfrac{T_{\text{high}}}{T_{\text{low}}}$	$\dfrac{\overline{n}_{\text{max}}}{\overline{n}_{\text{min}}}$
Cell A:						
I 1:	6.1	19.7	9		3.2	
2:	5.7(8)	20(2)	8.6(3)	0.62(2)		> 2.8
II 1:	7.3	31.1	12		4.3	
2:	7.3(6)	31(1)	12.5(1)	0.62(2)		> 3.4
III 1:	8.3	40.7	15		4.9	
2:	8(1)	41(1)	15.0(2)	0.63(4)		> 3.6
Cell B:						
I 1:	8.5	32.7	5		3.8	
2:	8.5(1)	33(1)	5.4(3)	0.62(5)		> 2

Fig. 7. Relative number density $\overline{n}(y)_{\Delta x}/\overline{n}(y_t = 43 \text{ mm})_{\Delta x}$ of setting III in gas cell A (cf. Table 1, $\Delta x = 35$ mm). #0: shadowed by the bottom plate, #1: affected by neutron reflection, #2: fit range for the forward calculation, #3: shadowed by the top plate. The error bars have been scaled to a reduced $\chi^2 = 1$ in region #2 ($\chi^2 = 1.17$ with 166 d.o.f. prior to scaling). The ratio $\overline{n}_{max}/\overline{n}_{min}$ in Table 1 (> 3.6) is defined from this diagram. The effective ratio 4.9 is not observable because of the divergent neutron paths.

The number density in cell A is constant for a given height, therefore the statistical error could be reduced by considering $\overline{n}(y_i)_{\Delta x}$, i.e. the average density at height y_i over a width Δx in x-direction. $\overline{n}(y_i)_{\Delta x}$ of setting III from Table 1 is compared to the forward calculation in Fig. 7 for $\Delta x = 35$ mm, i.e. 350 pixels.

In cell B the fraction of the data between bottom and top affected by neutron reflection increases with decreasing cell heights $h(x_{\text{cell}})$. The path length of the reflected neutrons is nearly the same compared to the non-reflected neutrons. Therefore reflected neutrons cannot obtain more than the maximal density or less than the minimal density along their path through the cell. A lower limit for the maximum to minimum density ratio between the top and bottom can still be extracted. The lower limit for the density ratio is 2 for a cell height $h(x_{\text{cell}}) < 10$ mm from the measurement in Table 1 (cf. Fig. 8).

6. Conclusion

In a neutron radiography experiment, a stationary cryogenic ^{3}He density distribution with maximum to minimum ratio exceeding a factor of 3 is verified. The gas density for different temperatures in the range from 6 K to 40 K at pressures around 10 mbar could be described to better than 2%. The thermal
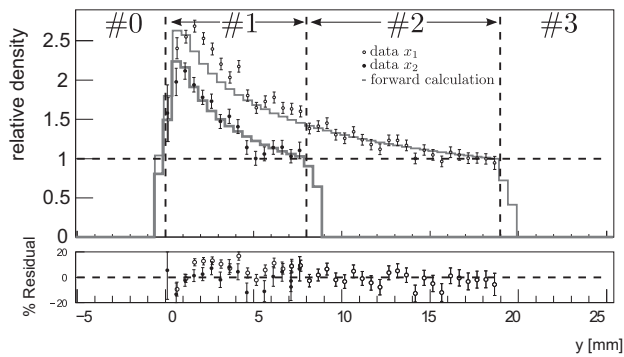
Fig. 8. Relative number density $\overline{n}(y)_{\Delta x}/\overline{n}(y_t = 19\,\text{mm})_{\Delta x}$ for the two lateral positions 'x_1' with 20 mm height and 'x_2' with 10 mm in Fig. 5 of gas cell B with setting in Table 1 ($\Delta x = 2$ mm). #0: shadowed by the bottom plate, #1: affected by neutron reflection, #2: fit range for the forward calculation. The error bars have been scaled to a reduced $\chi^2 = 1$ in region #2 ($\chi^2 = 1.23$ with 17 d.o.f. prior to scaling).

conductivity of ^{3}He gas was indirectly extracted over a descriptive parameterization.

The achieved density gradients can readily be transferred to a ^{4}He gas target and are suitable for the use in the muon cooling scheme of reference [4]. Together with the experimental demonstration of longitudinal cooling [5] this presents another essential step towards the realization of a high-quality low-energy μ^+ beam.

References

[1] A.D. Bross, Nuclear Physics B—Proceedings Supplements 229232 (2012) 529 (Neutrino, 2010).
[2] D. Taqqu, Detectors and Associated Equipment 247 (2) (1986) 288.
[3] M. Mühlbauer, H. Daniel, F. Hartmann, P. Hauser, F. Kottmann, C. Petitjean, W. Schott, D. Taqqu, P. Wojciechowski, Hyperfine Interactions 119 (1–4) (1999) 305.
[4] D. Taqqu, Physical Review Letters 97 (2006) 194801.
[5] Y. Bao, A. Antognini, W. Bertl, M. Hildebrandt, K.S. Khaw, K. Kirch, A. Papa, C. Petitjean, F.M. Piegsa, S. Ritt, K. Sedlak, A. Stoykov, D. Taqqu, Physical Review Letters 112 (2014) 224801.
[6] M.A. Barrufet, P.T. Eubank, Fluid Phase Equilibria 35 (1–3) (1987) 107.
[7] J.B. Mehl, Comptes Rendus Physique 10 (9) (2009) 859.
[8] A. Acton, K. Kellner, Physica B+C 90 (2) (1977) 192.
[9] E. Bich, R. Hellmann, E. Vogel, Molecular Physics 105 (23–24) (2007) 3035.
[10] V.F. Sears, Neutron News 3 (3) (1992) 26.
[11] H. Kobayashi, M. Satoh, Detectors and Associated Equipment 424 (1) (1999) 1.
[12] S. Tazaki, K. Neriishi, K. Takahashi, M. Etoh, Y. Karasawa, S. Kumazawa, N. Niimura, Detectors and Associated Equipment 424 (1) (1999) 20.